ACS Photonics

Article

pubs.acs.org/journal/apchd5

# Electro-Optics of Conventional and Inverted Thick Junction Organic Solar Cells

Ardalan Armin,*[,†] Aren Yazmaciyan,[†] Mike Hambsch,[†] Jun Li,[‡] Paul L. Burn,*[,†] and Paul Meredith*[,†]

[†]Centre for Organic Photonics & Electronics (COPE), School of Chemistry and Molecular Biosciences and School of Mathematics and Physics, The University of Queensland Brisbane 4072, Australia

[‡]Institute of Materials Research and Engineering, A*STAR, Singapore 117602, Singapore

Supporting Information

**ABSTRACT:** Bulk heterojunctions continue to be the dominant architecture for solution processed organic solar cells. In general, photoactive films on the order of 100 nm thickness have delivered the highest power conversion efficiencies. However, it is becoming increasingly apparent that thicker junctions are needed for high yield, high throughput, low cost manufacturing of commercial organic solar cells. Very few organic semiconductors are suitable for maintaining optimal efficiencies in cells with thicker junctions. This paradigm is beginning to shift with the recent high mobility donor polymers, where electrically inverted thick heterojunction structures deliver impressive efficiencies. The inverted architecture seems to be an essential feature of these solar cells. The reason for this has yet to be explained, and in this work, we address this question. We present analytical simulations and experimental evidence showing how the charge generation and extraction physics is significantly different in thin and thick heterojunctions, inverted and conventional. In particular, our predictive model shows how the inverted architecture compensates for strongly imbalanced carrier mobilities, which would otherwise cause debilitating recombination. Thick bulk heterojunctions can be designed to deliver high efficiencies, but for high mobility donors, this is only in an inverted architecture. These findings have profound implications for manufacturing of commercial organic solar cells.

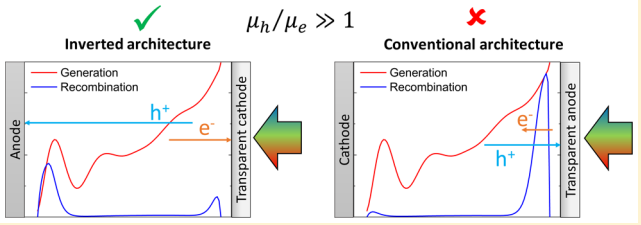


**KEYWORDS:** *organic solar cells, inverted solar cells, mobility balances, thick junctions, electro-optical properties*

Organic semiconductors can be solution processed, and this has driven significant interest for their deployment in next generation, low cost, low embedded energy optoelectronics, particularly solar cells. After significant effort, power conversion efficiencies exceeding 10% have now been achieved for laboratory scale devices, although at larger scale the performance is more modest due to a number of scaling physics issues.[1−5] The so-called bulk heterojunction (BHJ) architecture has emerged as the lead candidate for commercially viable solution processed organic solar cells, in which the active layer of the device consists of a blend of electron acceptor and donor organic semiconductors. Typically, in such BHJs, the junction thickness is restricted to around 100 nm (which we term thin), due to the fact that organic semiconductors are disordered excitonic materials with transport physics leading to the situation where bimolecular recombination is dominant at carrier densities typical of operational devices. This causes the charge extraction efficiency of a BHJ organic solar cell to rapidly deteriorate as a function of junction thickness. Unfortunately, thin junctions are not desirable from the perspective of delivering low cost, robust, high yield manufacturing of large area modules via techniques such as roll-to-roll coating or printing. Thin films are very prone to thickness variations and point defects, which scale exponentially with the area.[6] The apparent dichotomy between efficiency requirements and manufacturing viability is one of the main challenges holding back the scaling of organic solar cells.

There are only a relatively small number of organic semiconductor blend systems that maintain power conversion efficiencies (PCEs) in thick junctions. A classic example is the archetypal combination of regioregular poly(3-*n*-hexylthiophene) and [6,6]-phenyl-C61-butyric acid methyl ester (P3HT:PC60BM). This blend, if processed appropriately, can exhibit strongly suppressed bimolecular recombination, that is, non-Langevin with reduction factors of >100 relative to the Langevin rate.[7−9] However, the optical gap of the blend is defined by P3HT, which is ∼2 eV. This is far from optimal in terms of solar light harvesting, and this fact in combination with a relatively modest open circuit voltage (0.6−0.7 V) limits the PCE for this combination of materials to ∼3−5%.[10]

In addition to suppressed bimolecular recombination, the so-called "mobility balance" (i.e., the relative ratio of the slower to faster carrier mobilities) can also play an important role in achieving high PCEs in organic solar cells. We have previously reported on the need for balancing the electron and hole mobilities to maintain the Fill Factor (FF) in thick ($d$ > 300 nm) junction BHJs,[11] although mobility balance is not

**Received:** August 6, 2015
**Published:** November 25, 2015





DOI: 10.1021/acsphotonics.5b00441
*ACS Photonics* 2015, 2, 1745−1754

necessary in thin junctions.[12] This has also been confirmed through numerical device simulations reported by Bartelt et al.[13] More recently, there have been several reports on efficient thick junction BHJ solar cells using donor materials (polymeric and nonpolymeric) with narrow optical gaps and high hole mobilities. Power conversion efficiencies up to 8% have been achieved in devices with junction thicknesses of more than 300 nm.[4,14,15] The majority of these thick junctions, high efficiency devices use an electrically inverted architecture, where the transparent ITO (indium tin oxide) electrode acts as the cathode (extracting the electrons) in comparison with the conventional architecture where it functions as the anode. Notably, and in a direct analogy with the P3HT:PCBM system, the FF in these solar cells is maintained over a wide range of junction thicknesses. Thus, a question that needs to be addressed is whether the constant high FF is related to the inverted architecture, and if so, why?

In this communication, we present a model and numerical and experimental analysis of the role of the carrier mobility ratio ($\mu_h/\mu_e$) in defining the efficiency of thick junction organic solar cells. We utilize three BHJ blend systems with radically different mobility ratios ($\mu_h/\mu_e$ = 0.01, 1, 100) and study their electro-optics and performance metrics in thin and thick junctions, inverted and conventional. These three blend systems were P3HT:PC60BM with $\mu_h/\mu_e \approx 1$;[7] poly(*N*-9′-heptadecanyl-2,7-carbazole-*alt*-5,5-(4′,7′-di(thien-2-yl)-2′,1′,3′-benzothiadiazole)):[6,6]-phenyl-C71-butyric acid methyl ester (PCDTBT:PC70BM) with $\mu_h/\mu_e \approx 0.01$;[12] and poly[(2,5-{2-octyldodecyl}-3,6-diketopyrrolopyrrole)-*alt*-5,5-(2′,5′-di{thien-2-yl}thieno[3,2-*b*]thiophene)]:PC70BM (DPP-DTT:PC70BM), which exhibits $\mu_h/\mu_e \approx 100$.[16] We confirm that balanced mobilities (for example in the P3HT:PCBM system) maintain performance irrespective of conventional/inverted architectures. For $\mu_h/\mu_e \gg 1$, (i.e., a high hole mobility) the optimal FF and, hence, PCE are only achieved in thick junctions for an inverted architecture. Our electro-optical modeling shows this is because the device structure balances the electron and hole transit times creating symmetry in the collection efficiencies between the two carrier types. Conversely, for the more traditional case where $\mu_h/\mu_e \ll 1$, the inverted architecture actually increases the imbalance between the carrier transit times and decreases the PCE.

## THEORETICAL CONSIDERATIONS

**Photogenerated Carrier Profile in Thin and Thick Junction Solar Cells.** Upon illumination of an organic solar cell (typically through the transparent ITO electrode) light is absorbed in the semiconductor junction (the photoactive layer) and creates excitons. Free carrier generation via exciton dissociation is typically an ultrafast process (<ps) in bulk heterojunctions[17] and can be assumed to be instantaneous when compared with carrier transport that occurs over much longer time scales. Therefore, the distribution profile of light absorption within the active layer represents the charge generation profile $G(x)$. This, in turn, depends on the distribution of the optical field, $E(x)$, and absorption coefficient of the photoactive layer blend, $\alpha(\lambda)$, where $\lambda$ is the wavelength of the incident light. By assuming a perfect charge generation quantum yield, the charge generation profile for a given wavelength can be described by

$$G(x, \lambda) = \frac{1}{2h}\varepsilon_0\alpha(\lambda)n(\lambda)\lambda\,|E(x, \lambda)|^2 \quad (1)$$

where $h$ is the Planck's constant, $\varepsilon_0$ the vacuum permittivity, and $n$ the real part of the refractive index.[18] From eq 1 it is clear that to first order, the profile of the optical field $E(x, \lambda)$ defines the photocarrier generation distribution throughout the junction from electrode to electrode. $E(x, \lambda)$ is a function defined by how the light propagates in the photoactive layer (and in the optical thin film stack that comprises the entire solar cell) and can be determined by optical modeling methods such as transfer matrix calculations when all the layer thicknesses and their optical constants are known. Figure 1a shows the absorption spectrum of a typical photoactive layer, here PCDTBT:PC70BM (1:4 by weight) as a model example. The resultant photocarrier generation profiles at different wavelengths marked on the absorption spectrum in thick (700 nm, Figure 1b) and thin (80 nm, Figure 1c) junctions are also shown in Figure 1. These profiles were calculated by transfer matrix modeling under AM1.5G solar illumination for the simple solar cell structure described in the figure caption, and assuming an internal quantum efficiency (IQE) = 1. There are two important observations from these simulations: (i) in the thick junction, there are two absorption regimes: carriers are generated closer to the ITO surface (Beer−Lambert-like optical field distribution) for photons that have energies greater than the optical gap of the blend, and in the volume for those with energy around the absorption edge (cavity interference dominated optical field distribution); (ii) in the thin junction, the carriers are generated within the bulk (volume), regardless of the incident photon energy and thus, deliver qualitatively similar distribution profiles for all wavelengths. The difference

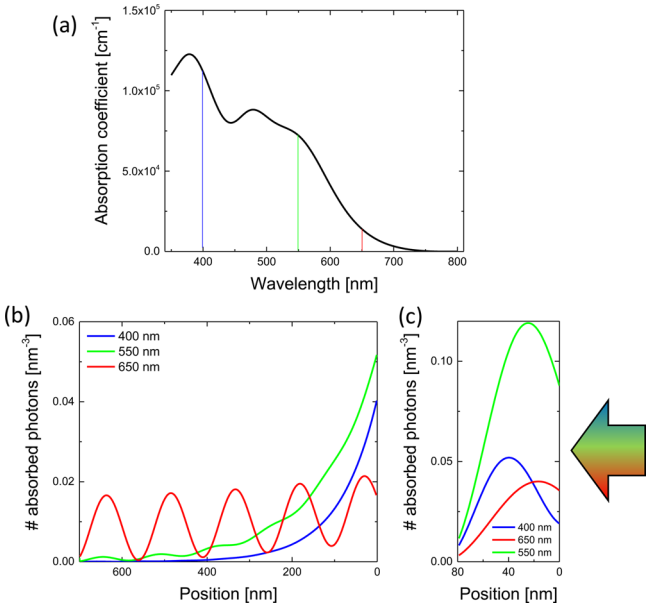


**Figure 1.** (a) Absorption coefficient of a PCDTBT:PC70BM thin film on glass (1:4 by weight). Photocarrier distribution profiles in 700 nm (b) and 80 nm (c) thick PCDTBT:PC70BM active layers in a solar cell structure comprising Al/PCDTBT:PC70BM/PEDOT:PSS/ITO/glass. In the thick junction case (b), the blue and green photons are mainly absorbed close to the ITO surface ($x$ < 200 nm) due to the large optical densities at those wavelengths, whereas the red photons can penetrate into the bulk and cause charge generation in the volume of the junction. In the thin junction (c), all wavelengths produce carrier distribution profiles more or less distributed throughout the volume of the film. PEDOT:PSS is poly(3,4-ethylenedioxythiophene):poly(styrene sulfonate).



DOI: 10.1021/acsphotonics.5b00441
*ACS Photonics* 2015, 2, 1745−1754

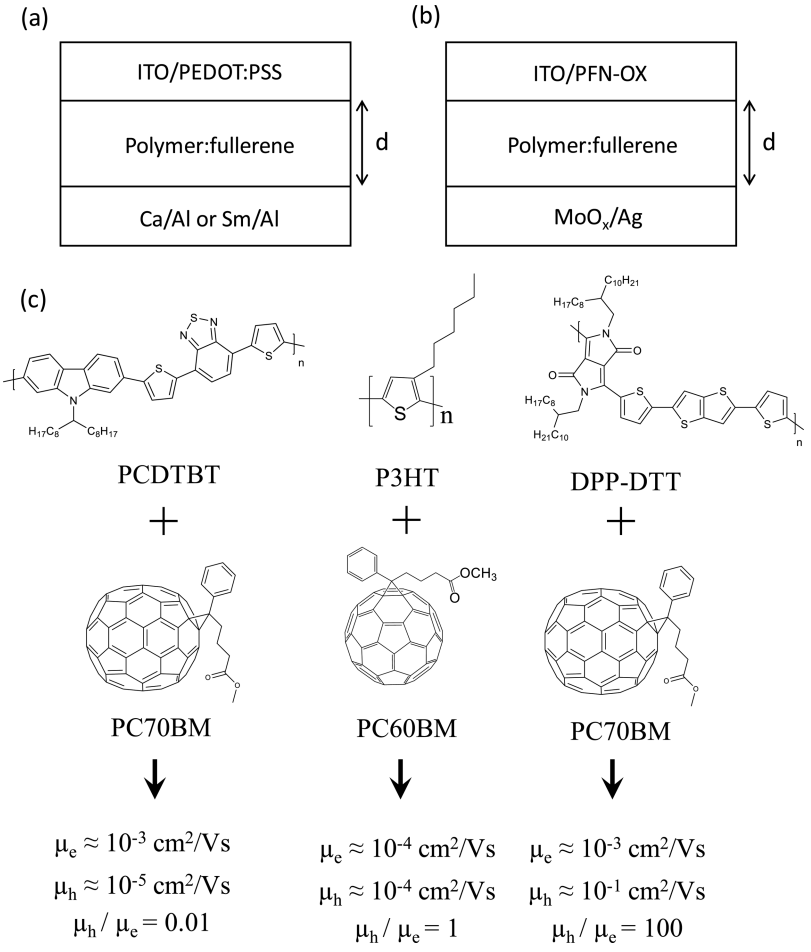


**Figure 2.** Device architectures used for numerical simulations and experimental investigations: (a) conventional and (b) inverted where d is the bulk heterojunction thickness. (c) Molecular structures of PCDTBT, P3HT, DPP-DTT (electron donors), and PC60BM and PC70BM (electron acceptors), and the electron and hole mobilities of their blends according to the recent literature.[11,12,16] Light is incident through the ITO/PEDOT:PSS transparent conducting anode in the conventional architecture and the ITO/PFN-OX cathode in the inverted architecture. PFN-OX is poly[(9,9-bis(6′-(*N*,*N*-dimethylamino)propyl)-2,7-fluorene)-*alt*-2,7-(9,9-bis(3-ethyl(oxetane-3-ethyloxy)-hexyl)-fluorene)].

between the carrier distribution profiles in the thin and thick junctions causes the charge carrier transport physics of the two cases to be systematically different.

**Mobilities and Transit Times in Thin and Thick Junctions.** Having established the photocarrier distribution profiles in thin and thick junctions, we now turn to the dynamics of their extraction, that is, the transport physics. Clearly, in the case of the thick junction for wavelengths dominated by Beer−Lambert absorption, electrons and holes have to travel very different distances to the cathode and anode, respectively. Depending upon the mobility ratio this should lead to an imbalanced transport. The preferential extraction of one carrier type is well-known to cause space charge of the slower species to build up.[12,19] The creation of space charge suppresses the overall charge carrier collection efficiency due to the screening of the built-in electric field. To probe these effects for inverted and conventional architectures, we utilize the so-called transit time $t_{tr}$ for both carrier types, that is, the time taken for a free carrier generated at a position $x_i$ to travel to the extracting electrode.

Based on this approach, we consider first a Beer−Lambert-like charge carrier distribution in a 700 nm thick model junction as shown in Figure 1b. The transit times for free electrons and holes generated at position $x_i$ can be written as

$$t_{tr}^{h} = \frac{x_i}{\mu_h E};\quad t_{tr}^{e} = \frac{d - x_i}{\mu_e E} \tag{2}$$

where $E$ denotes the internal electric field. Since the charges are distributed in space, it is appropriate to write the average transit time $\langle t_{tr} \rangle$ in terms of the average position of all photogenerated charges, $\langle x \rangle$:

$$\text{conventional: } \langle t_{tr}^{h} \rangle = \frac{\langle x \rangle}{\mu_h E};\quad \langle t_{tr}^{e} \rangle = \frac{d - \langle x \rangle}{\mu_e E} \tag{3}$$

$$\text{inverted: } \langle t_{tr}^{h} \rangle = \frac{d - \langle x \rangle}{\mu_h E};\quad \langle t_{tr}^{e} \rangle = \frac{\langle x \rangle}{\mu_e E} \tag{4}$$

where $\langle x \rangle$ can be written as

$$\langle x \rangle = \int_0^d x e^{-\alpha x} dx \Big/ \int_0^d e^{-\alpha x} dx \tag{5}$$

For a Beer−Lambert-like photocarrier distribution, as shown in Figure 1b, and in the case of large optical densities ($\alpha d \gg 1$), eqs 3−5 lead to the electron/hole transit time ratio

$$\text{conventional: } \frac{\langle t_{tr}^{e} \rangle}{\langle t_{tr}^{h} \rangle} = \frac{\mu_h}{\mu_e} \alpha d \tag{6}$$



DOI: 10.1021/acsphotonics.5b00441
*ACS Photonics* 2015, 2, 1745−1754

$$\text{inverted: } \frac{\langle t_{tr}^{e}\rangle}{\langle t_{tr}^{h}\rangle} = \frac{\mu_h}{\mu_e}\frac{1}{\alpha d} \tag{7}$$

Eqns 6 and 7 show that for thick junctions the difference in charge transport imbalance [exemplified through the transit time ratio, $(\langle t_{tr}^{e}\rangle/\langle t_{tr}^{h}\rangle)$] and mobility ratio $(\mu_h/\mu_e)$ are related via the optical density $(\alpha d)$. We thus make the following qualitative predictions for the three model systems with mobility ratios $\mu_h/\mu_e \ll 1$, $\mu_h/\mu_e \approx 1$, and $\mu_h/\mu_e \gg 1$:

*Conventional Architecture*. Condition 1: $\mu_h/\mu_e \ll 1$, charge transport becomes more balanced as the junction thickness increases; Condition 2: $\mu_h/\mu_e \gg 1$, charge transport becomes more imbalanced as junction thickness increases.

*Inverted Architecture*. Condition 3: $\mu_h/\mu_e \ll 1$, charge transport becomes more imbalanced as the junction thickness increases; Condition 4: $\mu_h/\mu_e \gg 1$, charge transport becomes more balanced as junction thickness increases.

These basic electro-optical considerations do not apply to thinner junctions where cavity interference dominates for all incident wavelengths. We now test these predictions numerically using the simple device architectures and materials shown in Figure 2.

## NUMERICAL SIMULATIONS

The material combinations shown in Figure 2 present one balanced (P3HT:PC60BM $\mu_h/\mu_e \approx 1$),[7] and two imbalanced mobility systems [$\mu_h/\mu_e \approx 0.01$ (PCDTBT:PC70BM)[12] and $\mu_h/\mu_e \approx 100$ (DPP-DTT:PC70BM)].[16] The optical constants[20,21] along with the electron and hole mobilities[7,12,16] of these blends have been measured and reported previously. The optical data are also provided in Figure S1. It is also important to note that these three systems exhibit nearly diffusion limited recombination rate constants (see refs 22, 23, and 24 for PCDTBT:PC70BM and P3HT:PC60BM, respectively). Figure S2 provides additional double injection transients (indicative of the recombination reduction factor)[7] for DPP-DTT:PC70BM, P3HT:PC60BM, and PCDTBT:PC70BM. These transients clearly demonstrate nearly diffusion limited recombination in these systems as no rise in the forward bias dark current can be observed. It should be noted that while a reference P3HT:PC60BM device annealed at a high temperature (180 °C) exhibits a rise in the forward bias dark current (indicative of accumulation of positive and negative charges due to suppressed recombination), our P3HT:PC60BM devices (annealed at 140 °C) show a constant current transient. In particular, the DPP-DTT:PC70BM system is interesting because it almost uniquely exhibits a higher hole mobility than electron mobility when appropriately processed at an optimum blend ratio to deliver solar cells with PCEs > 7%. To simulate the effect of architecture and junction thickness on photocarrier collection efficiency for these three mobility ratio conditions, we simulated the optical field distribution and determined the nongeminate recombination profile. Under steady state conditions, the spatial dependence of the photogenerated current density ($j$) can be derived from the following set of continuity equations

$$\frac{dj_n(x)}{dx} = -e[G(x) - R(x)] \tag{8}$$

$$\frac{dj_p(x)}{dx} = e[G(x) - R(x)] \tag{9}$$

where $G(x)$ is the sum of the photogenerated carrier densities integrated over all wavelengths within the solar spectral window, $R(x)$ is the bimolecular recombination rate, and $e$ the unit charge. $G(x)$ is dependent upon the incident light and optical properties of the solar cell, and is independent of the electrical properties of the system. It is a first order parameter and can be determined from eq 1 with appropriate optical simulations. For these simulations we used a code developed by Burkhard et al.[25] based on the transfer matrix method previously described.[26] The other two terms in eqs 8 and 9, the photocurrent density and recombination profiles, are dependent on the electrical properties of the system and were evaluated with the knowledge of $G(x)$ using a BHJ simulation code developed by Pierre et al.[27] In such an analysis, the recombination rate is assumed to be characteristically bimolecular such that

$$R(x) = \beta n(x)p(x) \tag{10}$$

where $n(x)$ and $p(x)$ are, respectively, the photogenerated electron and hole concentrations. The intrinsic carrier concentration is neglected since it is typically low in organic semiconductors compared to photogenerated carrier concentrations.[28] We have also assumed that the bimolecular recombination rate constant $\beta$ is dominated by the slower carrier mobility.[29] The photocurrent density can be written as a sum of the drift and diffusion currents for electrons and holes. These drift-diffusion equations for electrons and holes must be solved together with eqs 8 and 9 within the appropriate boundary conditions (set by the solar cell architecture) to obtain $R(x)$ and the photocurrent density profile. It is important to note that these simulations are qualitative, and do not provide absolute measures of the photocurrent and recombination. However, they are valuable for determining the relative spatial profiles.

Figure 3 shows the numerical simulation results for PCDTBT:PC70BM (Figure 3a,b), P3HT:PC60BM (Figure 3c,d), and DPP-DTT:PC70BM (Figure 3e,f) thin junction solar cells with an active layer thickness of ∼80 nm at short circuit under AM1.5G 1000 W/m$^2$ illumination. The photocarrier generation and recombination profiles were calculated for both inverted and conventional architectures. Although the mobility ratios for these three systems are very different, the recombination is negligible relative to the generation. In both cases and as depicted in Figure 1c, volume photogeneration dominates and there is no appreciable difference between the net free carrier profiles for the conventional versus inverted cells.

We now turn our attention to the cells with thick junctions (∼700 nm). Figure 4 shows the numerical simulation results for films of PCDTBT:PC70BM (Figure 4a,b), P3HT:PC60BM (Figure 4c,d), and DPP-DTT:PC70BM (Figure 4e,f), again for both conventional and inverted structures. In general, we see completely different behaviors than those observed in the thin junction devices. First, recombination in all cases is increased because of the substantially longer transit times. As predicted from the theoretical considerations, the location of the strongest recombination zone was defined by the architecture and mobility ratios. We shall return to this below on a case-by-case basis. Second, given that the conventional and inverted architectures are optically symmetrical, the photocarrier


DOI: 10.1021/acsphotonics.5b00441
ACS Photonics 2015, 2, 1745−1754

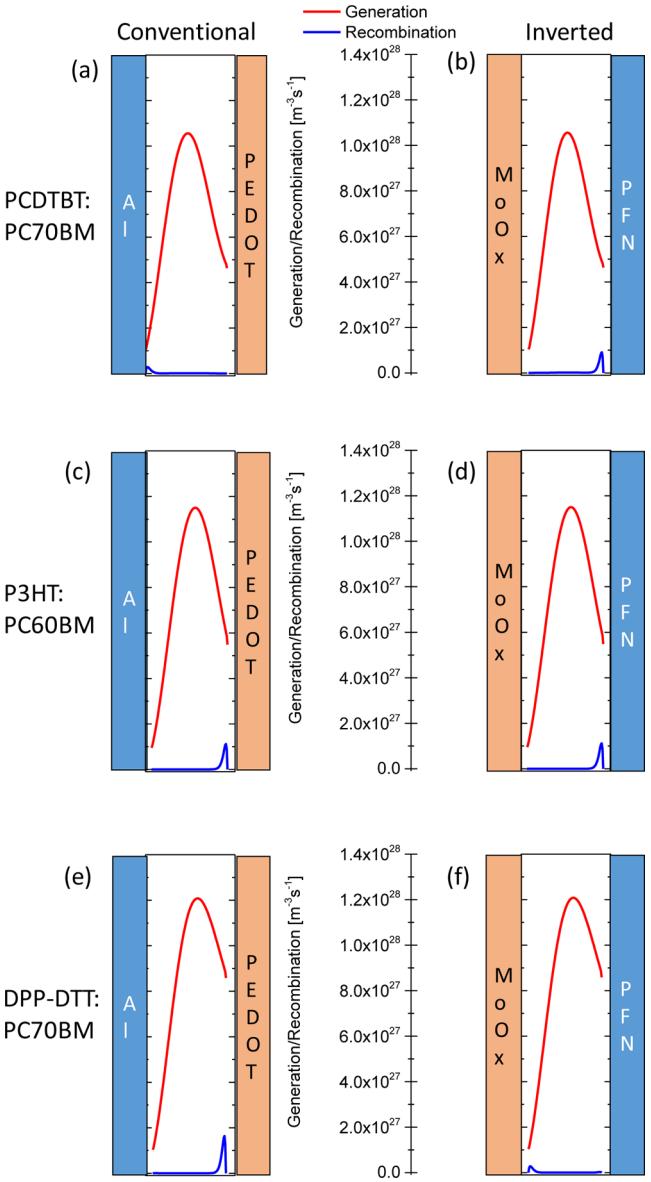


**Figure 3.** Numerical simulation results for photocarrier generation and recombination profiles in thin junction (~80 nm) PCDTBT:PC70BM (a, b), P3HT:PC60BM (c, d), and DPP-DTT:PC70BM (e, f) solar cells with electrically conventional (left panel) and inverted (right panel) architectures. In all cases, recombination is minimal compared to photogeneration, and both architectures deliver the same volume generated carrier profiles. The results were simulated at short circuit under AM1.5G illumination at 1000 W/m$^2$.

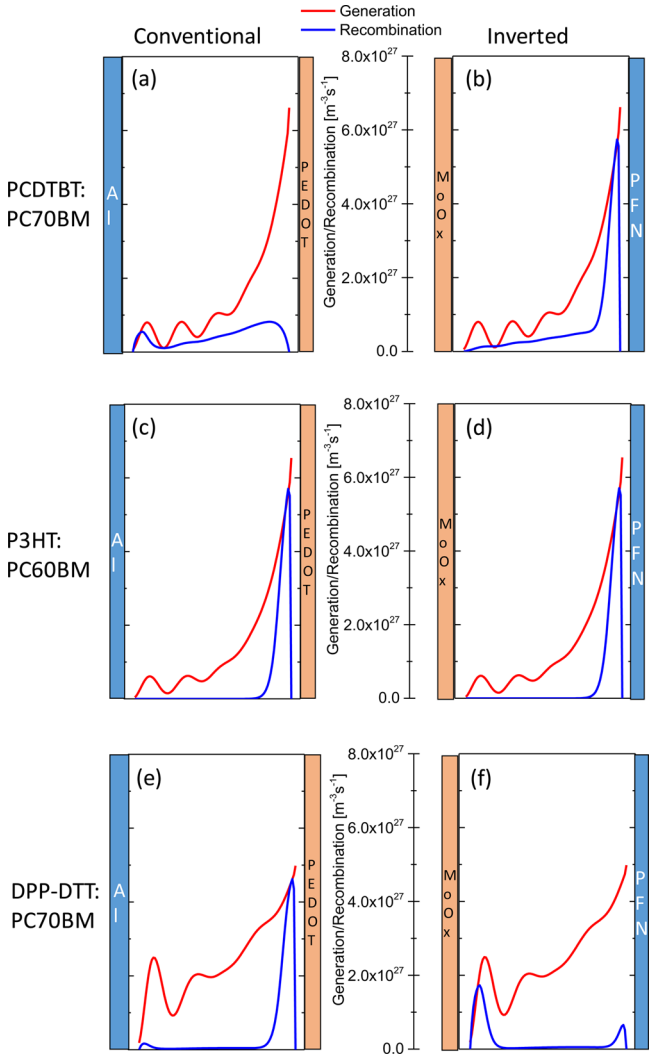


**Figure 4.** Numerical simulation results for photocarrier generation and recombination profiles in thick junction (~700 nm) PCDTBT:PC70BM (a, b), P3HT:PC60BM (c, d), and DPP-DTT:PC70BM (e, f) solar cells with electrically conventional (left panel) and inverted (right panel) architectures. The photocarrier generation and recombination profiles are dramatically different from the thin junction cases and individually dependent upon the mobility ratios and specific architectures. The results were simulated at short circuit under AM1.5G illumination at 1000 W/m$^2$.

generation profiles are likewise symmetrical and Beer–Lambert-like. In this regard, it is important to note the illumination direction: through the ITO/PEDOT:PSS transparent conducting anode in the conventional architecture; and the ITO/PFN-OX cathode in the inverted architecture. Generation in all cases near the transparent contact arises from blue-green photons, that is, where the film is strongly absorbing (Figure 1b). Photons of longer wavelengths where the film absorption is weaker, particularly near the blend absorption edges, do lead to some volume photocarrier generation and cavity interference signatures (fringes) near the reflecting electrode (Al or $MoO_x$/Ag).

For each of the film types we see the following recombination profiles:

PCDTBT:PC70BM ($\mu_h/\mu_e \ll 1$) Figure 4a,b: The inverted architecture shows very strong recombination near the nonreflecting electron extracting PFN-OX/ITO contact, coincident with the high photocarrier generation. This is in agreement with eq 7 and conditions 1 and 3, that is, the transit times (and hence transport) become more imbalanced in the inverted architecture as the junction thickness increases because of the low hole:electron mobility ratio. Hence, the conventional architecture solar cell should be superior in performance in the thick junction limit as the holes have less distance to travel.

P3HT:PC60BM ($\mu_h/\mu_e \approx 1$) Figure 4c,d: The conventional and inverted architectures show identical generation and recombination profiles. The situations are completely symmetrical and the zones of high recombination are coincident with high photocarrier generation near the transparent electrode (anode for the conventional architecture and cathode for the inverted). This is in agreement with the predictions of



DOI: 10.1021/acsphotonics.5b00441
ACS Photonics 2015, 2, 1745–1754

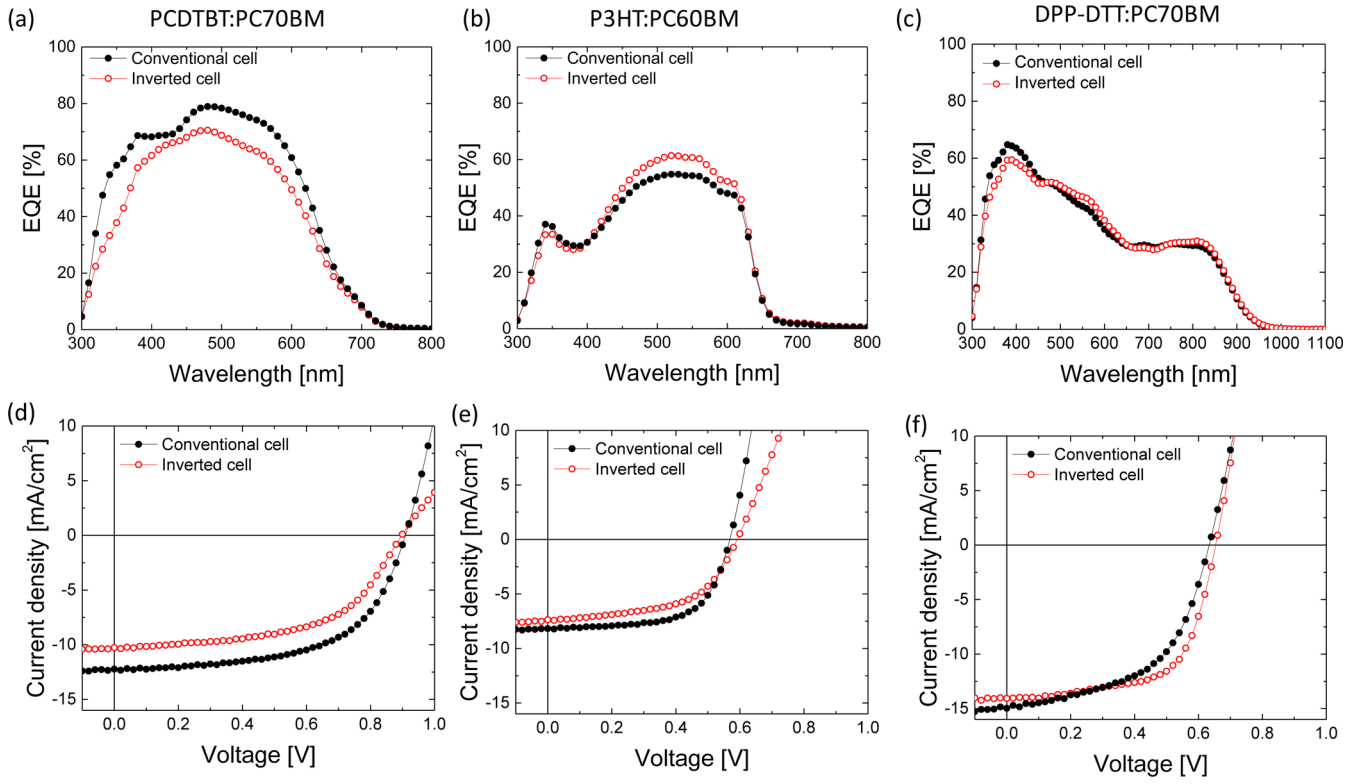


**Figure 5.** Representative external quantum efficiency spectra (EQEs; a–c) and $J$–$V$ characteristics (d–f) for conventional and inverted thin junction (~80 to 150 nm active layer thicknesses) PCDTBT:PC70BM, P3HT:PC60BM, and DPP-DTT:PC70BM bulk heterojunction solar cells. Device performance for each polymer/fullerene combination is architecture independent irrespective of the mobility balance.

**Table 1. Bulk Heterojunction Solar Cell Performance Metrics for the Different Device Architectures and Materials Shown in Figure 2**[a]

| | conventional cell | | | | inverted cell | | | |
|---|---|---|---|---|---|---|---|---|
| | $V_{OC}$ (V) | $J_{SC}$ (mA/cm$^2$) | FF | PCE (%) | $V_{OC}$ (V) | $J_{SC}$ (mA/cm$^2$) | FF | PCE (%) |
| PCDTBT:PC70BM | | | | | | | | |
| thick | 0.76 ± 0.02 | 8.1 ± 0.1 | 0.38 ± 0.00 | 2.3 ± 0.1 | 0.80 ± 0.01 | 1.6 ± 0.1 | 0.40 ± 0.00 | 0.5 ± 0.0 |
| thin | 0.89 ± 0.01 | 12.2 ± 0.2 | 0.59 ± 0.00 | 6.5 ± 0.0 | 0.88 ± 0.02 | 10.2 ± 0.2 | 0.56 ± 0.03 | 5.1 ± 0.3 |
| P3HT:PC60BM | | | | | | | | |
| thick | 0.54 ± 0.00 | 10.2 ± 0.2 | 0.50 ± 0.01 | 2.7 ± 0.0 | 0.52 ± 0.01 | 10.5 ± 0.1 | 0.46 ± 0.02 | 2.5 ± 0.2 |
| thin | 0.55 ± 0.01 | 7.9 ± 0.2 | 0.61 ± 0.02 | 2.7 ± 0.1 | 0.58 ± 0.02 | 7.4 ± 0.2 | 0.57 ± 0.03 | 2.5 ± 0.2 |
| DPP-DTT:PC70BM | | | | | | | | |
| thick | 0.57 ± 0.01 | 3.5 ± 0.5 | 0.53 ± 0.01 | 1.1 ± 0.1 | 0.62 ± 0.01 | 12.8 ± 0.2 | 0.55 ± 0.01 | 4.4 ± 0.1 |
| thin | 0.64 ± 0.01 | 14.1 ± 0.1 | 0.63 ± 0.01 | 5.7 ± 0.2 | 0.62 ± 0.00 | 14.7 ± 0.4 | 0.53 ± 0.03 | 4.9 ± 0.2 |

[a]Results are based on 10 devices for each case with a voltage scan from −1 to 1 V; ± represents standard deviations of the mean.

eqs 6 and 7. Hence, both architectures should deliver approximately equivalent performance.

DPP-DTT:PC70BM ($\mu_h/\mu_e \gg 1$) Figure 4e,f: The conventional architecture shows very strong recombination near the hole extracting transparent contact, coincident with the high photocarrier generation. This is in agreement with eq 6 and conditions 2 and 4, that is, the transit times (and hence, transport) become more imbalanced as the junction thickness increases in the conventional architecture because of the low electron mobility relative to the hole. Hence, the inverted architecture solar cell should be superior in performance in the thick junction limit as the electrons have less distance to travel.

## EXPERIMENTAL VALIDATION

We now move to test the theoretical predictions and numerical simulations experimentally in conventional and inverted, thin and thick junction cells with the materials and structures shown in Figure 2. Bulk heterojunction devices were fabricated and tested according to the standard procedures described in the Experimental Section. Figure 5 shows typical external quantum efficiency spectra (EQE) and current density–voltage ($J$–$V$) curves for conventional and inverted thin junction PCDTBT:PC70BM (Figure 5a,d), P3HT:PC60BM (Figure 5b,e), and DPP-DTT:PC70BM (Figure 5c,f) solar cells. Optimized junction thicknesses between ~80 and 150 nm were used. Within experimental error and considering the fact that the conventional and inverted cells contain different electrode materials, it can be seen that for each of the blends the two architectures deliver very similar performance. Accurate device statistics with appropriate standard deviations of the mean are presented in Table 1. Thus, the experimental results confirm the theoretical predictions and numerical simulations



DOI: 10.1021/acsphotonics.5b00441
ACS Photonics 2015, 2, 1745–1754

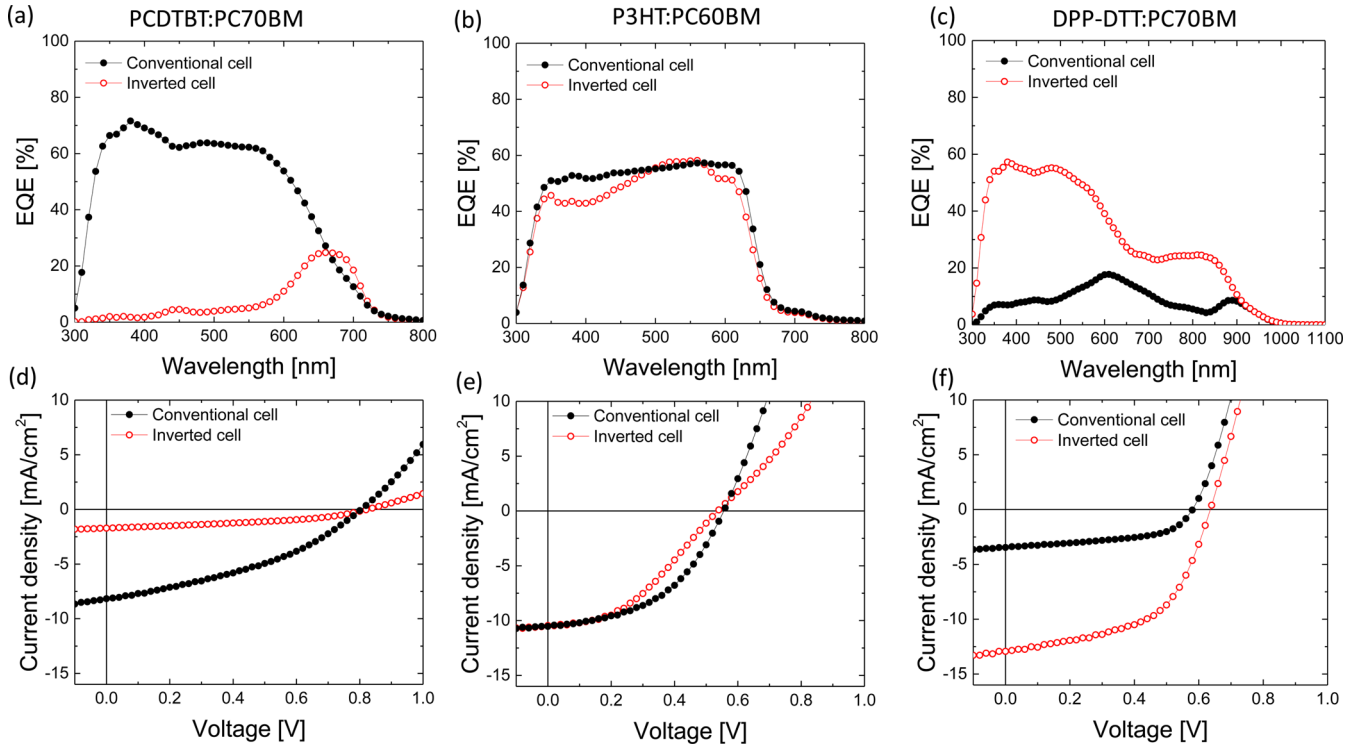


**Figure 6.** External quantum efficiency spectra (a–c) and $J-V$ characteristics (d–f) of conventional and inverted thick junction (~600–700 nm) PCDTBT:PC70BM, P3HT:PC60BM, and DPP-DTT:PC70BM solar cells. For the PCDTBT:PC70BM system with $\mu_h/\mu_e \ll 1$, the conventional device performs significantly better compared to the inverted one. In the case of DPP-DTT:PC70BM solar cells with $\mu_h/\mu_e \gg 1$, the conventional cell exhibits very poor EQE, while the inverted device operates more efficiently with a higher EQE and photocurrent. As a result of $\mu_h/\mu_e \approx 1$ for the P3HT:PC60BM blends, both conventional and inverted structure devices generate the same photocurrent and show similar performances.

for the thin junction solar cells, in that the performance is independent of architecture and mobility balance.

Figure 6 presents representative EQE spectra and $J-V$ curves for thick junction (and ~600–700 nm active layer) PCDTBT:PC70BM (Figure 6a,d), P3HT:PC60BM (Figure 6b,e), and DPP-DTT:PC70BM (Figure 6c,f) solar cells both in conventional and inverted architectures. In contrast to the thin junction devices, there are marked differences between the inverted and conventional structures, and it is instructive to consider each of these in turn noting full device statistics are summarized for completeness in Table 1.

PCDTBT:PC70BM ($\mu_h/\mu_e \ll 1$) Figure 6a,d: In the conventional architecture, this blend delivers a relatively flat, >60% EQE indicating that all wavelengths absorbed contribute essentially equally to charge generation. That is, the holes and higher mobility electrons can be extracted from the device. This is in agreement with previous reports of an incident energy independent charge generation quantum yield in the system[20,21] and high charge collection efficiency (low recombination) as expected for conventional thick junction structures with $\mu_h/\mu_e \ll 1$ (Figure 4a, eq 7, condition 1). The inverted architecture however exhibits low photocurrent (low EQE) due to the dramatically increased recombination induced by the imbalanced transport. The EQE appears almost fully suppressed in the blue and green parts of the spectrum with a narrow peak in the red. These observations are in good accordance with the simulations of Figure 4b, and the predictions of eq 6 and condition 3 with substantial and debilitating recombination occurring near the transparent cathode. It is clear for the thick junction case, where $\mu_h/\mu_e \ll 1$, the conventional architecture delivers higher PCEs. We would also note that control of the EQE spectral shape, in this case restricting photocurrent generation to a narrow window in the red, was recently exploited by Armin et al. to develop narrowband red and near-infrared photodiodes using thick bulk heterojunctions.[30] The authors termed the concept "charge collection narrowing" reflecting the underlying mechanism of manipulating the charge collection efficiency using the same physics described here.

P3HT:PC60BM ($\mu_h/\mu_e \approx 1$) Figure 6b,e: For the case of balanced mobilities both EQEs and white light $J-V$s are similar. Once again, the thick junction EQEs are relatively flat across the solar spectrum indicative of energy independent charge generation and collection in this system. These results confirm blends with balanced mobilities are architecturally insensitive in line with the predictions of eqs 6 and 7 and the simulations of Figure 4c,d.

DPP-DTT:PC70BM ($\mu_h/\mu_e \gg 1$) Figure 6c,f: In this case, the inverted architecture delivers a far higher EQE and correspondingly superior white light $J-V$. We see relative suppression of the EQE in the red part of the spectrum, which is due to the inefficient photoinduced electron transfer from the polymer to fullerene in this system as previously reported by Armin et al.,[21] and consistent with stronger recombination near the reflecting electrode as predicted (Figure 4f, eq 7, condition 4). The EQE in the conventional architecture is very low indicative of strong recombination near the transparent anode due to the space charge build-up of electrons (Figure 4e, eq 6, condition 2). Thus, as predicted, for the thick junction case $\mu_h/\mu_e \gg 1$, the inverted architecture delivers higher PCEs.



DOI: 10.1021/acsphotonics.5b00441
ACS Photonics 2015, 2, 1745–1754

## CONCLUSION

The majority of high efficiency bulk heterojunction organic solar cells to date have contained thin junctions of order 100 nm thickness. Thick junction devices with only a few exceptions lose Fill Factor and PCE due to increased recombination. This is problematic from the perspective of large area manufacturing since thin junctions are susceptible to point defects and active layer thickness inhomogeneity. A growing number of reports are emerging of high mobility donor organic semiconductors that deliver impressive thick junction performance in combination with fullerene electron acceptors, but mostly in the electrically inverted architecture. We have studied the electro-optics of this phenomenon in three model systems with different carrier mobility ratios: PCDTBT:PC70BM ($\mu_h/\mu_e \ll 1$); P3HT:PC60BM ($\mu_h/\mu_e \approx 1$); and DPP-DTT:PC70BM ($\mu_h/\mu_e \gg 1$). We present a simple theoretical model backed by numerical simulations and direct experimental evidence to explain why the inverted architecture is a necessary requirement when the electron is the slower carrier in a thick junction. The essence of this model is that when $\alpha d \gg 1$ (the thick junction limit), the inverted architecture assists in balancing the electron and hole transit times, that is, it creates balanced transport even when there is a strong mobility imbalance. Based upon this insight, one can define a set of design guidelines to assist in creating new materials and architectures for thick bulk heterojunction organic solar cells with more viable manufacturing potential in large area photovoltaic modules, namely:

(i) For thin junctions, where all incident wavelengths generate photocarriers in the volume, inverted and conventional architectures will produce similar power conversion efficiencies;
(ii) For balanced mobilities ($\mu_h/\mu_e \approx 1$), cell efficiencies can be maintained in thick junctions, and the conventional and inverted architectures should deliver equivalent performance being optically and electrically symmetrical;
(iii) For imbalanced mobilities where the electron is the faster carrier ($\mu_h/\mu_e \ll 1$), the conventional architecture partially rebalances the transport and will be superior to the inverted architecture;
(iv) For imbalanced mobilities where the hole is the faster carrier ($\mu_h/\mu_e \gg 1$), the inverted architecture delivers high efficiencies in thick junctions by rebalancing the transport; the conventional architecture has the opposite effect and enhances the debilitating effects of the mobility imbalance.

## EXPERIMENTAL SECTION

**Materials and Device Fabrication.** The solar cells were fabricated on prepatterned indium tin oxide (ITO) glass substrates (15 Ω $sq^{-1}$: Xinyan) in a class 1000 clean room. The substrates were cleaned in a detergent bath (Alconox) at 80 °C for 10 min and mechanically cleaned by a soft cloth, followed by sonication in sequence with Alconox, deionized water, acetone, and 2-propanol for 10 min each. The cleaned substrates were dried with nitrogen before spin-coating the subsequent layers. For conventional cells, a 30 ± 5 nm thick PEDOT:PSS (Heraeus Clevios P VP AI 4083) layer was deposited by spin-coating at 5000 rpm for 30 s, whereas a PFN-OX solution (0.5 mg/mL in methanol with 1% acetic acid v/v) was deposited by spin-coating at 2000 rpm for 20 s to form a ∼5 nm thick hole blocking layer for electrically inverted cells. The PEDOT:PSS coated substrates were baked at 165 °C for 10 min, while those with the PFN-OX layer were baked at 150 °C for 20 min to achieve cross-linking of the layer.[15] After cooling down, the substrates were transferred into a nitrogen-filled glovebox for device fabrication ($O_2$ < 1 ppm, $H_2O$ < 1 ppm). PCDTBT ($\bar{M}_w$ = 122.2 kDa, PDI = 5.4, SJPC Canada) and PC70BM (American Dye Source) were both dissolved in anhydrous 1,2-dichlorobenzene (DCB) at 150 and 80 °C, respectively. The PCDTBT solution was then cooled down to 80 °C within ∼30 min. The PC70BM solution was filtered at room temperature before being added to the PCDTBT solution to give a weight ratio of 1:4 at 80 °C. The final mixture was cooled down to ambient temperature by switching off the hot plate. The solution was filtered through glass wool before being deposited by spin-coating onto the substrates. The total concentrations of the solutions to obtain 80 and 700 nm thick films by spin coating at 1200 and 500 rpm were 22.5 and 35 mg/mL, respectively. For the P3HT:PC60BM devices, 30 mg of PC60BM (American Dye Source) was dissolved in 1 mL of DCB at 70 °C and then stirred at room temperature overnight. The PC60BM solution was then filtered before adding 30 mg of P3HT and the final mixture was left on the hot plate at 70 °C for 1 h. The blend solution was spin-coated once it had cooled down to room temperature within ∼15 min. The 90 nm thick films were deposited by spin-coating 15 mg/mL solutions at 600 rpm, whereas the 60 mg/mL solution was spin-coated at 350 rpm in order to form 600−700 nm thick films. Finally, to fabricate the DPP-DTT:PC70BM solar cells, the DPP-DTT ($\bar{M}_w$ = 350 kDa, PDI = 2.8)[31] and PC70BM were dissolved individually in chloroform containing 7% DCB by volume at 60 °C. The solutions were then mixed at 50 °C to obtain two different solutions with total concentrations of 15 and 30 mg/mL with a ratio of 1:3 by weight for thin and thick junctions, respectively. Active layers for thin (∼150 nm) and thick (∼700 nm) junction devices were deposited at 1000 and 700 rpm, respectively. All the films consisting of different polymer/fullerene blends were baked at 50 °C for 5 min after spin-coating of the active layers as a part of an additional solvent evaporation process. Finally, the metal electrodes (Ca, Sm, $MoO_x$, Al, and Ag) were deposited by thermal evaporation under a $10^{-6}$ mbar vacuum with an appropriate mask to achieve a device area of 0.2 $cm^2$. P3HT:PC60BM devices were also annealed at 140 °C for 5 min after the metal evaporation.

**Current Density−Voltage Measurements and External Quantum Efficiency Measurements.** Current density−voltage ($J-V$) characteristics were acquired for unencapsulated devices in a nitrogen-filled glovebox using a Keithley 2400 Source Measure Unit and Agilent B1500A semiconductor analyzer. The simulated Air Mass 1.5 Global (AM 1.5 G) illumination was provided by an Abet Sun 2000 Solar Simulator. The intensity used throughout was ∼1000 W/$m^2$ (the exact number being used for efficiency calculations), as determined by an NREL-calibrated silicon reference cell. External quantum efficiency (EQE) spectra and the near normal incidence reflectance of the devices were recorded with a PV Measurements Inc. QEX7 system, which was calibrated with a NREL certified photodiode without light bias.

## ASSOCIATED CONTENT

### Supporting Information

The Supporting Information is available free of charge on the ACS Publications website at DOI: 10.1021/acsphotonics.5b00441.



DOI: 10.1021/acsphotonics.5b00441
ACS Photonics 2015, 2, 1745−1754

Optical constants of PCDTBT:PC70BM, P3HT:PC60BM, and DPP-DTT:PC70BM and double injection current transients of solar cells made of these three systems (PDF).

## AUTHOR INFORMATION


### Corresponding Authors

*E-mail: p.burn2@uq.edu.au.
*E-mail: meredith@physics.uq.edu.au.
*E-mail: a.armin@uq.edu.au.


### Notes

The authors declare no competing financial interest.

## ACKNOWLEDGMENTS

This Program was funded by the Australian Government through the Australian Renewable Energy Agency (ARENA) Australian Centre for Advanced Photovoltaics. Responsibility for the views, information, or advice expressed herein is not accepted by the Australian Government. P.L.B. is a UQ Vice Chancellor's Research Focused Fellow and P.M. is an ARC Discovery Outstanding Researcher Award Fellow. A.Y. is supported by a University of Queensland International scholarship (UQI). We thank Prof. Fei Huang and Zhicheng Hu from the South China University of Technology for supplying PFN-OX. This work was performed in part at the Queensland node of the Australian National Fabrication Facility (ANFF), a company established under the National Collaborative Research Infrastructure Strategy to provide nano- and microfabrication facilities for Australia's researchers.

## REFERENCES


(1) Green, M. A.; Emery, K.; Hishikawa, Y.; Warta, W.; Dunlop, E. D. Solar cell efficiency tables (Version 45). *Prog. Photovoltaics* **2015**, *23*, 1−9.

(2) He, Z.; Xiao, B.; Liu, F.; Wu, H.; Yang, Y.; Xiao, S.; Wang, C.; Russell, T. P.; Cao, Y. Single-junction polymer solar cells with high efficiency and photovoltage. *Nat. Photonics* **2015**, *9*, 174−179.

(3) Huang, J.; Li, C.-Z.; Chueh, C.-C.; Liu, S.-Q.; Yu, J.-S.; Jen, A. K. Y. 10.4% Power Conversion Efficiency of ITO-Free Organic Photovoltaics Through Enhanced Light Trapping Configuration. *Adv. Ener. Mater.* **2015**, *5*, 1500406.

(4) Liu, Y.; Zhao, J.; Li, Z.; Mu, C.; Ma, W.; Hu, H.; Jiang, K.; Lin, H.; Ade, H.; Yan, H. Aggregation and morphology control enables multiple cases of high-efficiency polymer solar cells. *Nat. Commun.* **2014**, *5*, 5293.

(5) Sun, K.; Xiao, Z.; Lu, S.; Zajaczkowski, W.; Pisula, W.; Hanssen, E.; White, J. M.; Williamson, R. M.; Subbiah, J.; Ouyang, J.; Holmes, A. B.; Wong, W. W. H.; Jones, D. J. A molecular nematic liquid crystalline material for high-performance organic photovoltaics. *Nat. Commun.* **2015**, *6*, 6013.

(6) Krebs, F. C. Fabrication and processing of polymer solar cells: A review of printing and coating techniques. *Sol. Energy Mater. Sol. Cells* **2009**, *93*, 394−412.

(7) Armin, A.; Juska, G.; Philippa, B. W.; Burn, P. L.; Meredith, P.; White, R. D.; Pivrikas, A. Doping-Induced Screening of the Built-in-Field in Organic Solar Cells: Effect on Charge Transport and Recombination. *Adv. Ener. Mater.* **2013**, *3*, 321−327.

(8) Moulé, A. J.; Bonekamp, J. B.; Meerholz, K. The effect of active layer thickness and composition on the performance of bulk-heterojunction solar cells. *J. Appl. Phys.* **2006**, *100*, 094503.

(9) Zeng, L.; Tang, C. W.; Chen, S. H. Effects of active layer thickness and thermal annealing on polythiophene: Fullerene bulk heterojunction photovoltaic devices. *Appl. Phys. Lett.* **2010**, *97*, 053305.

(10) Dang, M. T.; Hirsch, L.; Wantz, G. P3HT:PCBM, Best Seller in Polymer Photovoltaic Research. *Adv. Mater.* **2011**, *23*, 3597−3602.

(11) Armin, A.; Hambsch, M.; Wolfer, P.; Jin, H.; Li, J.; Shi, Z.; Burn, P. L.; Meredith, P. Efficient, Large Area, and Thick Junction Polymer Solar Cells with Balanced Mobilities and Low Defect Densities. *Adv. Ener. Mater.* **2015**, *5*, 1401221.

(12) Armin, A.; Juska, G.; Ullah, M.; Velusamy, M.; Burn, P. L.; Meredith, P.; Pivrikas, A. Balanced Carrier Mobilities: Not a Necessary Condition for High-Efficiency Thin Organic Solar Cells as Determined by MIS-CELIV. *Adv. Ener. Mater.* **2014**, *4*, 1300954.

(13) Bartelt, J. A.; Lam, D.; Burke, T. M.; Sweetnam, S. M.; McGehee, M. D. Charge-Carrier Mobility Requirements for Bulk Heterojunction Solar Cells with High Fill Factor and External Quantum Efficiency >90%. *Adv. Ener. Mater.* **2015**, *5*, 1500577.

(14) Li, W.; Hendriks, K. H.; Roelofs, W. S. C.; Kim, Y.; Wienk, M. M.; Janssen, R. A. J. Efficient Small Bandgap Polymer Solar Cells with High Fill Factors for 300 nm Thick Films. *Adv. Mater.* **2013**, *25*, 3182−3186.

(15) Hu, X.; Yi, C.; Wang, M.; Hsu, C.-H.; Liu, S.; Zhang, K.; Zhong, C.; Huang, F.; Gong, X.; Cao, Y. High-Performance Inverted Organic Photovoltaics with Over 1-$\mu$m Thick Active Layers. *Adv. Ener. Mater.* **2014**, *4*, 1400378.

(16) Armin, A.; Wolfer, P.; Shaw, P. E.; Hambsch, M.; Maasoumi, F.; Ullah, M.; Gann, E.; McNeill, C. R.; Li, J.; Shi, Z.; Burn, P. L.; Meredith, P. Simultaneous enhancement of charge generation quantum yield and carrier transport in organic solar cells. *J. Mater. Chem. C* **2015**, *3*, 10799−10812.

(17) Clarke, T. M.; Durrant, J. R. Charge Photogeneration in Organic Solar Cells. *Chem. Rev.* **2010**, *110*, 6736−6767.

(18) Pettersson, L. A. A.; Roman, L. S.; Inganäs, O. Modeling photocurrent action spectra of photovoltaic devices based on organic thin films. *J. Appl. Phys.* **1999**, *86*, 487−496.

(19) Mihailetchi, V. D.; Wildeman, J.; Blom, P. W. M. Space-Charge Limited Photocurrent. *Phys. Rev. Lett.* **2005**, *94*, 126602.

(20) Armin, A.; Velusamy, M.; Wolfer, P.; Zhang, Y.; Burn, P. L.; Meredith, P.; Pivrikas, A. Quantum Efficiency of Organic Solar Cells: Electro-Optical Cavity Considerations. *ACS Photonics* **2014**, *1*, 173−181.

(21) Armin, A.; Kassal, I.; Shaw, P. E.; Hambsch, M.; Stolterfoht, M.; Lyons, D. M.; Li, J.; Shi, Z.; Burn, P. L.; Meredith, P. Spectral Dependence of the Internal Quantum Efficiency of Organic Solar Cells: Effect of Charge Generation Pathways. *J. Am. Chem. Soc.* **2014**, *136*, 11465−11472.

(22) Clarke, T. M.; Peet, J.; Nattestad, A.; Drolet, N.; Dennler, G.; Lungenschmied, C.; Leclerc, M.; Mozer, A. J. Charge carrier mobility, bimolecular recombination and trapping in polycarbazole copolymer: fullerene (PCDTBT: PCBM) bulk heterojunction solar cells. *Org. Electron.* **2012**, *13*, 2639−2646.

(23) Jin, H.; Armin, A.; Hambsch, M.; Lin, Q.; Burn, P. L.; Meredith, P. Bulk heterojunction thickness uniformity−a limiting factor in large area organic solar cells? *Phys. Status Solidi A* **2015**, *212*, 2246−2254.

(24) Clarke, T. M.; Ballantyne, A. M.; Nelson, J.; Bradley, D. D.; Durrant, J. R. Free energy control of charge photogeneration in polythiophene/fullerene solar cells: the influence of thermal annealing on P3HT/PCBM blends. *Adv. Funct. Mater.* **2008**, *18*, 4029−4035.

(25) Burkhard, G. F.; Hoke, E. T.; McGehee, M. D. Accounting for Interference, Scattering, and Electrode Absorption to Make Accurate Internal Quantum Efficiency Measurements in Organic and Other Thin Solar Cells. *Adv. Mater.* **2010**, *22*, 3293−3297.

(26) Peumans, P.; Yakimov, A.; Forrest, S. R. Small molecular weight organic thin-film photodetectors and solar cells. *J. Appl. Phys.* **2003**, *93*, 3693−3723.

(27) Pierre, A.; Lu, S.; Howard, I. A.; Facchetti, A.; Arias, A. C. Empirically based device modeling of bulk heterojunction organic photovoltaics. *J. Appl. Phys.* **2013**, *113*, 154506.

(28) Morfa, A. J.; Nardes, A. M.; Shaheen, S. E.; Kopidakis, N.; van de Lagemaat, J. Time-of-Flight Studies of Electron-Collection Kinetics in Polymer:Fullerene Bulk-Heterojunction Solar Cells. *Adv. Funct. Mater.* **2011**, *21*, 2580−2586.




DOI: 10.1021/acsphotonics.5b00441
*ACS Photonics* 2015, 2, 1745−1754

(29) Koster, L. J. A.; Mihailetchi, V. D.; Blom, P. W. M. Bimolecular recombination in polymer/fullerene bulk heterojunction solar cells. *Appl. Phys. Lett.* **2006**, *88*, 052104.
(30) Armin, A.; Jansen-van Vuuren, R. D.; Kopidakis, N.; Burn, P. L.; Meredith, P. Narrowband light detection via internal quantum efficiency manipulation of organic photodiodes. *Nat. Commun.* **2015**, *6*, 6343.
(31) Li, J.; Zhao, Y.; Tan, H. S.; Guo, Y.; Di, C.-A.; Yu, G.; Liu, Y.; Lin, M.; Lim, S. H.; Zhou, Y. A stable solution-processed polymer semiconductor with record high-mobility for printed transistors. *Sci. Rep.* **2012**, *2*, 754.



DOI: 10.1021/acsphotonics.5b00441
*ACS Photonics* 2015, 2, 1745−1754